

Intermittent Turbulence in the Stable Boundary Layer over Land. Part III: A Classification for Observations during CASES-99

B. J. H. VAN DE WIEL, A. F. MOENE, O. K. HARTOGENESIS, H. A. R. DE BRUIN, AND A. A. M. HOLTSLAG

Department of Meteorology and Air Quality, Wageningen University, Wageningen, Netherlands

(Manuscript received 22 July 2002, in final form 21 November 2002)

ABSTRACT

In this paper a classification of stable boundary layer regimes is presented based on observations of near-surface turbulence during the Cooperative Atmosphere-Surface Exchange Study-1999 (CASES-99). It is found that the different nights can be divided into three subclasses: a turbulent regime, an intermittent regime, and a radiative regime, which confirms the findings of two companion papers that use a simplified theoretical model (it is noted that its simplified structure limits the model generality to near-surface flows). The papers predict the occurrence of stable boundary layer regimes in terms of external forcing parameters such as the (effective) pressure gradient and radiative forcing. The classification in the present work supports these predictions and shows that the predictions are robust in a qualitative sense. As such, it is, for example, shown that intermittent turbulence is most likely to occur in clear-sky conditions with a moderately weak effective pressure gradient. The quantitative features of the theoretical classification are, however, rather sensitive to (often uncertain) local parameter estimations, such as the bulk heat conductance of the vegetation layer. This sensitivity limits the current applicability of the theoretical classification in a strict quantitative sense, apart from its conceptual value.

1. Introduction

On clear nights with weak winds, a frequently observed phenomenon is the weak and intermittent character of turbulence in the atmospheric boundary layer. Intermittent turbulence is characterized by brief episodes of turbulence with intervening periods of relatively weak or unmeasurably small fluctuations (Mahrt 1999). Despite its common nature, relatively little is known about the physical mechanisms behind the intermittent turbulence in the stable boundary layer (SBL). Intermittency can be generated by several physical mechanisms (see Van de Wiel et al. 2002a): by local shear effects (Ha and Mahrt 2001), by instability on the scale of the entire surface inversion layer, or by turbulence generated aloft diffusing to the surface [see the review on SBL issues by Mahrt (1999)]. Also, locally produced waves formed by Kelvin-Helmholtz instabilities could play a role in triggering turbulence bursts [e.g., Coulter 1990; Nappo 1991; also recently observed during the Cooperative Atmosphere-Surface Exchange Study-1999 (CASE-99; Poulos et al. 2002)].

In the present work and in the companion papers of Van de Wiel et al. [2002a,b, hereafter VdW(a,b)], we focus on an intermittency mechanism, which results

from a direct interaction between the lower atmosphere and the surface, in presence of a pressure gradient. According to this mechanism, described in detail in VdW(a,b), intermittency is generated by an alternating sequence of SBL collapse (cessation of turbulence) as a consequence of strong surface cooling, followed by a recovery of the SBL (generation of turbulence). The recovery is induced by acceleration of the air by the pressure gradient during the collapse period (period of reduced friction). This increases the shear until $Ri < R_c$, eventually providing the condition for turbulent mixing (Businger 1973; Turner 1973). It is noted that in VdW(a,b), interaction with higher shear levels (as in Ha and Mahrt 2001) was not considered, which may limit the generality of the present results.

In VdW(a) the physical essentials of the mechanism described above were extracted, resulting in a model system of three coupled nonlinear differential equations. As such it was shown that this truncated model was able to mimic the observed intermittent turbulence. Also, the model simulated *both* an intermittent and two nonintermittent regimes for different parameter ranges, resulting in three different regimes for clear-sky conditions. Furthermore, the simplified model essentially showed the same behavior as more complex models (e.g., Blackadar 1979; Lin 1990; Revelle 1993; McNider et al. 1995).

In a second paper, VdW(b), the model equations were studied analytically following a system dynamics ap-

Corresponding author address: Dr. B. J. H. Van de Wiel, Dept. Of Meteorology and Air Quality, Duivendaal 2, Wageningen University, Wageningen 6701 AP, Netherlands.
E-mail: Bas.vandeWiel@wur.nl

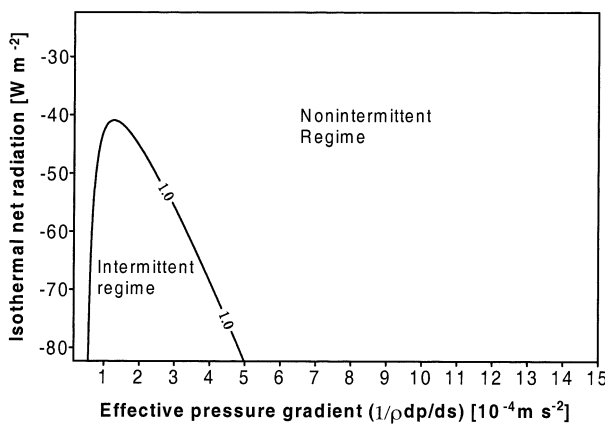


FIG. 1. Classification of SBL regimes in terms of external parameters. The figure represents a contour plot of Π values. Only one contour line is drawn, namely that of the critical level $\Pi = 1$. Within this line ($\Pi < 1$) intermittent cases are predicted, and nonintermittent cases are predicted outside this line ($\Pi > 1$).

proach. This resulted in a dimensionless parameter (denoted as Π), which was shown to be a predictor of the equilibrium behavior (e.g., intermittent or nonintermittent) of the simplified system. This critical parameter Π is merely a function of *external “forcings/parameters,”* such as the pressure gradient and the radiative forcing and of local properties, such as surface roughness, surface heat conductance, and surface heat capacity. As such, this parameter was proposed as a classification tool to predict intermittent and nonintermittent SBL regimes. It was shown that $\Pi < 1$ corresponds to intermittent situations and $\Pi \geq 1$ corresponds to nonintermittent cases.

For a specific location with fixed local properties the dependence of Π on external forcings can be drawn in a *classification diagram*, valid for that location. An example is given in Fig. 1 showing the critical level $\Pi = 1$ as a contour line for different values of the effective pressure gradient and of the isothermal net radiation Q_i . The isothermal net radiation is a measure for the radiative forcing (section 2), such that the upper part of Fig. 1 indicates cloudy conditions and the lower part corresponds to clear skies. According to the Π concept, all cases within the contour line $\Pi < 1$ correspond to nocturnal boundary layers with intermittent turbulence, and all cases outside the contour line $\Pi > 1$ correspond to nonintermittent cases. It is observed that under clear-sky conditions, three regimes are predicted, occurring at different values of the effective pressure gradient. This confirms the earlier findings from model simulations by VdW(a). For cloudy cases, only a single nonintermittent (i.e., continuous turbulent) regime is predicted.

With the theoretical work of VdW(a,b) as a point of departure, the present work investigates recent observations of SBL regimes during CASES-99. As such, the main goal of the present paper is to

- 1) classify the different nights of the CASES-99 field experiment into subregimes (section 3) based on flux time series (with a focus on near-surface measurements), wherein a key question is, Can we distinguish three different regimes as predicted?;
- 2) determine the value of Π for each night by using observations (section 4) wherein a key question is, Where would the CASES-99 nights be located in terms of Fig. 1?;
- 3) compare the classification based on this Π concept (using “external” parameters) with the independent classification based on observed flux time series (i.e., using internal variables; section 5).

The extensive cooperative field experiment CASES-99 was carried out by various groups from the United States and Europe in Kansas, in October 1999 (see this issue and Poulos et al. 2002). The experiment lasted for an entire month, under *various meteorological conditions*, which makes it extremely suitable to study different SBL regimes in relation to the external forcings.

The paper is organized as follows. In section 2, a short data description is given. Sections 3, 4, and 5 address objectives 1, 2, and 3 (above), respectively. Discussion and conclusions follow in sections 6 and 7.

2. Data description

The CASES-99 stable boundary layer experiment took place during October 1999, 50 km east of Wichita, Kansas. The experimental area, covered with dry, open prairie grass (0–0.25 m high), was relatively flat with some minor slopes in the order of 0.5 degrees. A vast array of instruments was deployed. For a general description of the experiment we refer to Poulos et al. (2002) and to the official CASES-99 Internet site at <http://www.colorado-research.com/cases/CASES-99.html> (data freely available).

The Meteorology Group of Wageningen University provided observations at one point ($37^{\circ}38.611'N$, $96^{\circ}44.233'W$) in a nested network of flux stations around the central 55-m flux tower of the National Center for Atmospheric Research (NCAR). An eddy covariance system was set up at a height of 2.65 m and operated at 20 Hz. It consisted of a Campbell Scientific model CSAT3 sonic anemometer and model KH2O Krypton hygrometer. Raw data were stored on a laptop and processed as described in Hartogensis et al. (2002). In order to get detailed information about the temporal variation of the fluxes (section 3) a rather short averaging period of 5 min was chosen. Comparison with 30-min-averaged fluxes (not shown) gave little systematic difference, favoring the use of a short averaging period. At the same time it is recognized that, especially in very stable conditions, accurate flux estimations from sonic anemometers is not trivial, due to the fact that pathlength may not be small compared to (typical) eddy

size. This problem is, however, not discussed here (see, e.g., Moore 1986).

Shortwave radiation components were measured with a CM14 albedometer and longwave radiative components by a CG2 pyrgeometer (both manufactured by Kipp and Zonen), mounted on a tripod at 1.5 m. From these radiation components the net radiation was calculated. Two soil heat flux plates were employed (at -0.054 m; one manufactured by TNO; the other a REBS model HFT3) together with two Pt-100 soil thermometers (at -0.028 and -0.080 m; provided by Wageningen University). Both radiation and soil measurements were sampled at 5 s and averaged and stored every 10 min (on a Campbell Scientific 21X micrologger). For a more detailed description of all the measurements by the Wageningen Group, we refer to the Web site above.

The height of the turbulent boundary layer was inferred from sodar observations [returned signal strength (in decibels)] at Beaumont, Whitewater, and Oxford as part of the Argonne National Laboratory Boundary Layer Experiment (ABLE) program infrastructure (see Pouloos et al. 2002).

3. Observed flow regimes during CASES-99

a. Method

In this section a classification based on observations of flux time series is made. This time series classification will be compared with the theoretical predictions using the classification diagram in section 5. The different nights are divided into classes according to the typical characteristics of their turbulent heat flux time series. The turbulent heat flux near the surface is chosen as indicator because the turbulent heat flux is directly influenced by two external key parameters: the synoptic pressure gradient and the isothermal net radiation (section 4). We note that our current flux analysis focuses on near-surface measurements, which may limit the generality of the results (see discussion).

From numerical simulations by VdW(a) and the analytical work by VdW(b), it became clear that three typical time traces of the turbulent heat flux are to be expected: 1) a regime with high turbulent transport and nonintermittent fluxes, 2) a regime with intermittent fluxes, 3) a regime with very low turbulent transport and nonintermittent fluxes. These theoretically predicted traces are used as a guideline for the time series classification introduced below. It will be shown that the time series could easily be evaluated by eye because the different regimes show very different behavior. In order to avoid subjectivity, only clear examples were classified (a priori) as such (see below).

b. Results: A classification of SBL regimes using observation of flux time series

From the time series of the surface fluxes (H and u_*) during the observational period, it is found that the

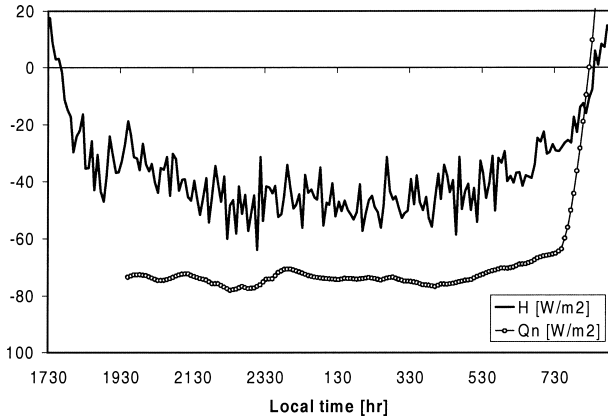


FIG. 2. A typical example of a time series of the sensible heat flux and net radiation during a continuous turbulent night (14–15 Oct).

CASES-99 nights (indeed) can be subdivided into the following regimes:

- 1) continuous turbulent regime,
- 2) intermittent regime,
- 3) radiative regime.

To illustrate the main features of each class, typical examples are given below.

1) CONTINUOUS TURBULENT NIGHTS

In Fig. 2 the turbulent heat flux is shown during a clear night with continuous turbulence (14–15 October). The sensible heat flux reaches a large value of about -45 W m^{-2} , due to strong radiative surface cooling ($Q_{\text{net}} \approx -75 \text{ W m}^{-2}$) in combination with strong turbulent mixing ($u_* \approx 0.5 \text{ m s}^{-1}$).

2) INTERMITTENT NIGHTS

In Figs. 3a,b two typical examples of intermittent nights are given. These examples give an impression about the typical timescales and amplitudes of the turbulent events and the quiet periods. It is observed that they are rather irregular. Some turbulent periods have very small amplitudes of 5 W m^{-2} and timescales of less than 10 min; others have amplitudes of 25 W m^{-2} and a duration of 4 h. The quiet periods may, but need not, result in a total decay of the flux, and the timescales also range from tens of minutes to a few hours.

An interesting result is given by the net radiation graphs of Figs. 3a,b, showing small deviations superimposed on a smooth decreasing trend (absolute value). The smooth trend results from a strong surface cooling during the night. The small deviations are caused by the turbulent bursts, leading to alterations of the surface temperature which immediately affects the net radiation [cf. model simulations by VdW(a)].

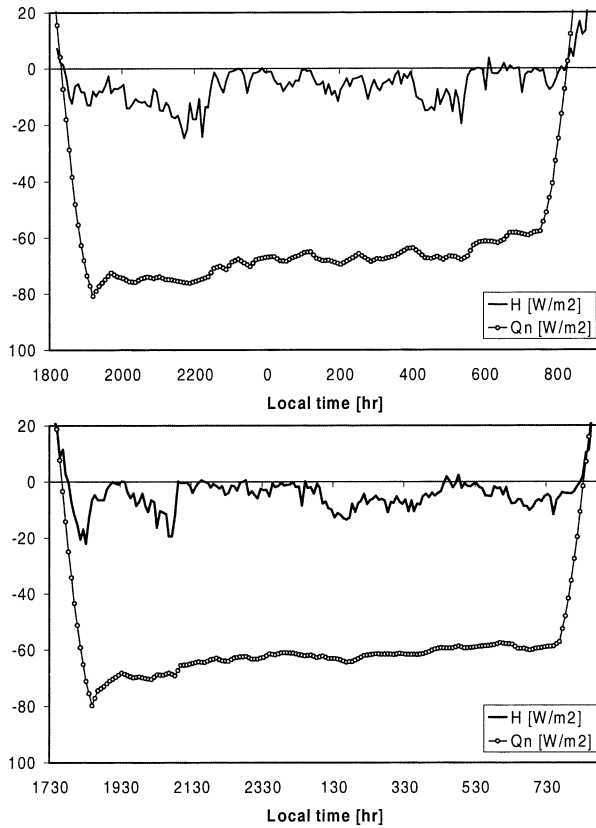


FIG. 3. Typical examples of the sensible heat flux and net radiation for two nights with intermittent turbulence: (top) 4–5 Oct and (bottom) 23–24 Oct.

3) RADIATIVE NIGHTS

In contrast to the well-mixed case of Fig. 2, a night with hardly any turbulent heat flux is shown in Fig. 4. Because the transport of energy through the atmosphere by turbulence is so small, we indicate these nights simply as “radiative nights.”

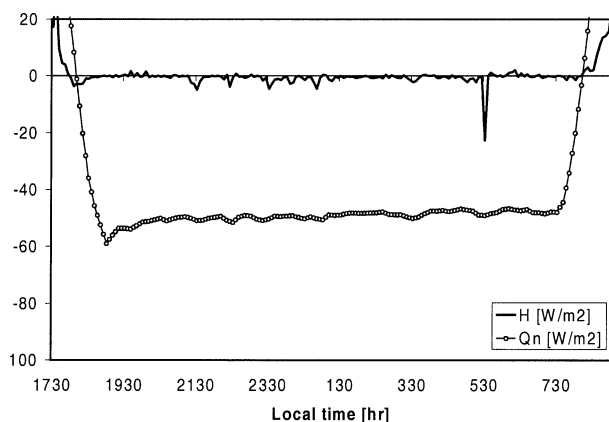


FIG. 4. A typical example of a time series of the sensible heat flux and net radiation during a radiative night (9–10 Oct).

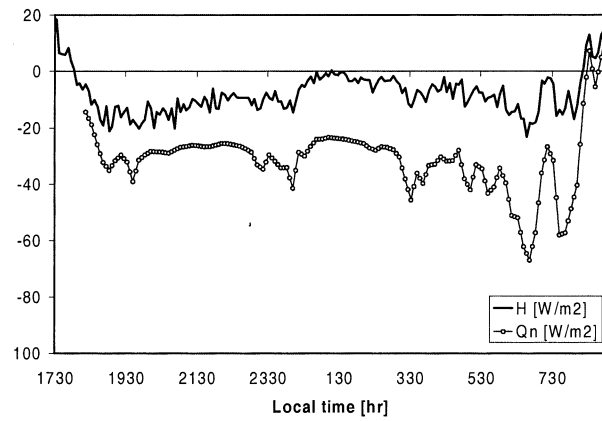


FIG. 5. Sensible heat flux and net radiation in a night with varying cloud cover (16–17 Oct).

4) A CLOUDY CASE

Contrary to the previous clear-sky examples, in Fig. 5 (16–17 October), a night with variable cloud cover is shown. In this case the turbulent heat flux demonstrates alternating higher and lower values. From this heat flux graph only, it looks as if this could be a night with intermittent turbulence. On the contrary, however, *it is a night with continuous turbulence*, as will be shown below. In the following, Fig. 5 is compared with Fig. 3a (4–5 October). Comparing the net radiation graphs of both figures, it is observed that the magnitude of the net radiation during 16–17 October is much smaller and more variable than during 4–5 October, indicating the presence of clouds in the first place. The contrast between the two nights becomes more evident in the friction velocity graphs (Fig. 6). In the intermittent situation (4–5 October) the values of u_* are very low and correlated with H . In the continuous turbulent case (16–17 October), the values of u_* are high and not correlated with H . These examples show that in the cloudy night the radiative factors are limiting for the turbulent heat

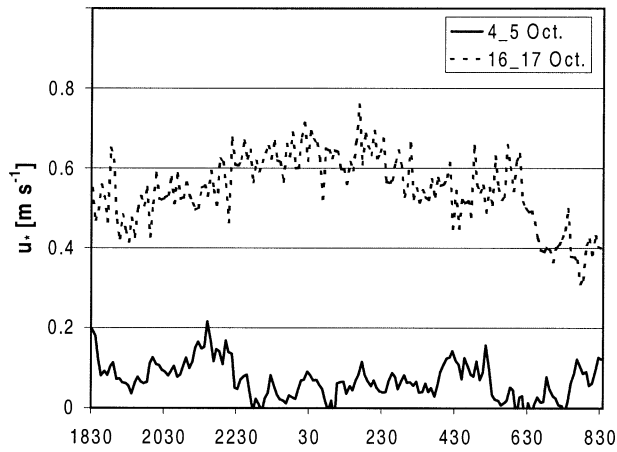


FIG. 6. Comparison of friction velocity time series during an intermittent and during a nonintermittent night.

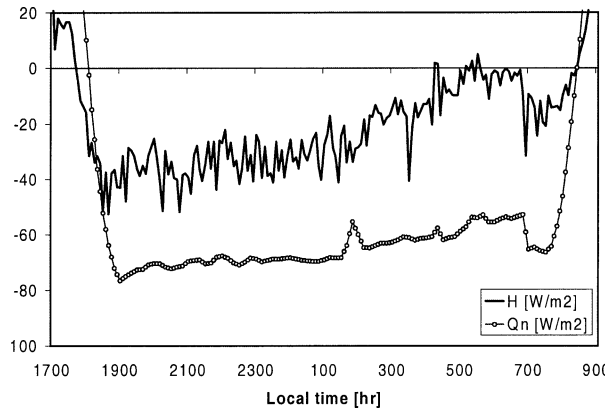


FIG. 7. Sensible heat flux and net radiation during a night with transient behavior (12–13 Oct).

flux, whereas in the clear night the mixing efficiency is the limiting factor for the turbulent heat flux. In terms of K theory, in the cloudy case the temperature gradient is the limiting factor (negative feedback mechanism), whereas in the clear-sky, intermittent case the turbulent diffusivity is limiting [positive feedback mechanism; De Bruin 1994; Derbyshire 1999; VdW(b)].

5) A TRANSIENT CASE

In the previous examples the behavior of near-surface turbulence was classified into three different regimes. It is realized that any SBL classification is only a simplification of real SBL complexity (Mahrt et al. 1998). This fact is illustrated by an example of a transient night given in Fig. 7. In the beginning of the night, the figure seems a perfect example of a night with continuous turbulence. After 0200 LST, however, it is observed that the heat flux H rapidly decreases from about -40 W m^{-2} to almost zero. This collapse of turbulence was also clearly visible in u_* (not shown) decreasing from about 0.35 m s^{-1} around 0 h to 0.05 m s^{-1} around 0600 LST. Apart from some influence of high-level clouds, the net radiation remains rather large. Around 0700 LST (40 min before sunrise) a sudden recovery of H and u_* (increasing from 0.02 – 0.22 m s^{-1} within 5 min) occurs. It seems that rapidly changing synoptic conditions strongly influenced the mechanical budget of the SBL. Several of these kinds and other transitional cases, were observed during CASES-99. In this study these cases are not classified explicitly but are indicated as *transient* or “*nonclassified*” cases.

c. Classification applied to the whole CASES-99 dataset

The classification of the previous section was applied to the whole CASES-99 data period. The results of this time series classification are summarized in Table 1. Also in Table 1, the mean values of some basic micro-

meteorological variables are given to indicate typical values occurring at different conditions/regimes. The averages were calculated over 0000–0600 LST. This period is chosen because it is often the most stationary period of the night (contrary to the period after sunset), although a purely stationary period [as assumed in VdW(b)] in its strict sense that the variables do not change in time, is not reached.

From Table 1, it occurs that 20 out of 28 nights were classified. Of these 20 classified nights, 8 nights (40%) showed continuous turbulence during the 6-h period, 8 nights (40%) showed intermittent turbulence, and 4 nights (20%) behaved as a radiative nights. From these frequency statistics, the number of intermittent and radiative nights may seem rather high compared to the number of turbulent nights. This can be explained by the large number of clear nights during the CASES-99 field campaign (Poulos et al. 2002). It is well known that clear-sky conditions favor moderately to strongly stable SBLs that may lead to radiative or intermittent nights. In more cloudy conditions the number of intermittent/radiative nights will be less.

Although a detailed discussion about the micrometeorological characteristics of each night is beyond the scope of this paper, some general characteristics are outlined.

- As expected, turbulent nights mostly occur in situations with strong winds and weak inversions. In the same way, intermittent and radiative nights tend to occur in low wind conditions with stronger temperature inversions.
- Most of the nights show large net radiation indicating clear nights.
- From the mechanical point of view, a large range in u_* values (0.02 – 0.59 m s^{-1}) is observed, leading to a broad range of stability conditions.
- Mostly, the latent heat flux is small.
- Generally speaking, the magnitude of the soil heat flux (SHF) is large compared to the other terms in the energy balance, showing the importance of this process. Therefore, a detailed description of the SHF measurements and its analysis are given in the appendix, together with some innovative results. Because the complete set of SHF instruments by Wageningen University was only available at the end of the experiment, only this part of the measurements is given.

4. Application of II: Input parameters

a. Introduction

In this section the dimensionless Π number [VdW(b)] is evaluated for each night to predict the particular SBL regime for that night. Thus, for each night, the input parameters have to be estimated from the data, which is not a trivial task, in view of the simplified character of the theoretical model. Therefore, we discuss the pa-

TABLE 1. Classification of CASES-99 nights based on turbulent heat flux observations. Also, an overview of some basic micrometeorological variables is given (6-h averages). “**Trans.**” is for transient; “**Turb.**” is for turbulent, “**Int.**” is for intermittent, and “**Rad.**” is for radiative. (Source, Meteorology Group of Wageningen University.)

DOY (-)	Date (-)	Time [LST (h)]	Class (-)	u^* (m s ⁻¹)	Q_{net} (W m ⁻²)	H (W m ⁻²)	LvE (W m ⁻²)	G (W m ⁻²)	U_{10} (m s ⁻¹)	T_{10} (K)	T_s (K)
274	1 Oct	0000–0600	Trans.	0.150	-65.8	-23.4	4.5	—	3.42	285.27	282.57
275	2 Oct	0000–0600	Trans.	0.267	-35.2	-15.9	16.4	—	4.68	286.65	285.70
276	3 Oct	0000–0600	Turb.	0.295	-6.2	7.0	18.8	—	4.46	281.30	282.44
277	4 Oct	0000–0600	Trans.	0.213	-49.3	-2.9	2.3	—	3.76	276.99	277.36
278	5 Oct	0000–0600	Int.	0.061	-66.8	-5.9	-0.5	—	3.29	279.97	277.08
279	6 Oct	0000–0600	Int.	0.075	-61.7	-6.9	-2.2	—	2.82	285.16	281.41
280	7 Oct	0000–0600	Turb.	0.438	-71.2	-48.4	14.8	—	6.40	288.80	286.57
281	8 Oct	0000–0600	Int.	0.139	-48.3	-10.1	-5.6	—	3.15	287.49	285.82
282	9 Oct	0000–0600	Int.	—	—	—	—	—	—	—	—
283	10 Oct	0000–0600	Rad.	0.022	-48.6	-1.2	-0.6	—	2.03	288.62	284.45
284	11 Oct	0000–0600	Turb.	0.360	-65.8	-32.7	10.0	—	5.59	288.94	287.20
285	12 Oct	0000–0600	Turb.	0.217	-64.3	-20.4	-2.1	—	4.05	290.38	287.91
286	13 Oct	0000–0600	Trans.	0.199	-62.5	-17.5	-1.8	—	3.67	290.38	288.10
287	14 Oct	0000–0600	Rad.	0.031	-62.8	-1.4	-0.3	—	2.26	281.50	278.71
288	15 Oct	0000–0600	Turb.	0.494	-73.9	-45.6	5.7	—	7.21	292.79	290.41
289	16 Oct	0000–0600	Turb.	0.451	-58.9	-13.8	9.2	—	7.45	285.44	285.24
290	17 Oct	0000–0600	Turb.	0.594	-31.2	-5.7	12.5	-24.0	9.30	282.63	283.04
291	18 Oct	0000–0600	Int.	0.094	-55.6	-4.1	2.9	-39.7	2.97	277.02	275.01
292	19 Oct	0000–0600	Rad.	0.033	-57.6	-1.1	0.4	-45.1	2.14	279.87	276.65
293	20 Oct	0000–0600	Int.	0.070	-61.9	-5.7	0.1	-38.9	3.06	278.11	275.17
294	21 Oct	0000–0600	Trans.	0.115	-63.2	-14.3	-0.2	-32.1	3.94	283.37	279.19
295	22 Oct	0000–0600	Trans.	0.119	-60.7	-17.7	3.2	-30.9	4.50	286.16	280.68
296	23 Oct	0000–0600	Trans.	0.172	-70.1	-19.3	3.1	-42.6	4.35	278.86	276.71
297	24 Oct	0000–0600	Int.	0.067	-61.2	-4.8	0.5	-48.3	2.92	275.02	273.12
298	25 Oct	0000–0600	Turb.	0.296	-69.6	-34.5	3.9	-29.5	6.28	282.11	279.45
299	26 Oct	0000–0600	Rad.	0.018	-53.4	-1.7	-0.3	-39.6	2.02	285.29	277.64
300	27 Oct	0000–0600	Int.	0.158	-65.4	-27.8	0.0	-28.9	3.81	288.12	283.35
301	28 Oct	0000–0600	Trans.	0.230	-59.6	-28.9	0.3	—	4.19	287.97	285.28

rameters in relation to the available data, which will result in an overview table of input parameters and Π numbers. Due to its extremely complex form, the explicit form of the Π parameter is not discussed here. For the exact analytical form of Π and its derivation we refer to [VdW(b)].

b. Estimation of external forcing parameters

1) THE EFFECTIVE PRESSURE GRADIENT

VdW(a) showed that in the theoretical model, an *effective* value of the pressure gradient is used rather than the “real” pressure gradient, due to the negligence of Coriolis effects. Here, the effective pressure gradient is defined as the pressure gradient in the direction of the mean wind speed in the lower atmosphere. In practice it is not straightforward to estimate this effective value accurately.

- The mean wind direction close to the surface may vary in time, especially in conditions of intermittent turbulence, where changes in surface friction cause changes in the (cross isobaric) flow direction up to tens of degrees. This affects the effective component of the pressure gradient.
- In the SBL the “mean” wind may vary considerably with height (e.g., Nieuwstadt and Tennekes 1981), which makes it difficult to choose a single “repre-

sentative” mean wind direction for the lower atmosphere.

- Often, from weather maps only limited time intervals with pressure data are available (e.g., each 6 h), whereas the pressure gradient may vary during these intervals.

Therefore, a different approach is followed in order to obtain a measure for the effective pressure gradient. The point of departure is the momentum budget of the mean wind speed following the model of VdW(a,b):

$$\frac{\partial U}{\partial t} = - \left(\frac{1}{\rho} \frac{\partial P}{\partial s} \right)_{\text{effective}} - \frac{u_*^2}{h}. \quad (1)$$

In this equation the influence of advection was neglected. Furthermore, a “classical” boundary layer structure was assumed (as, e.g., in Nieuwstadt 1984) where the stress decreases gradually with height until it vanishes at the boundary layer top. If the assumption of stationarity is adopted as well (as in the original derivation of Π), then the effective pressure gradient can be replaced by

$$- \left(\frac{1}{\rho} \frac{\partial P}{\partial s} \right)_{\text{effective}} = \frac{u_*^2}{h}. \quad (2)$$

This substitution is applied to Fig. 1 (Fig. 8). Note that the shape of Fig. 8 is unchanged compared to Fig. 1.

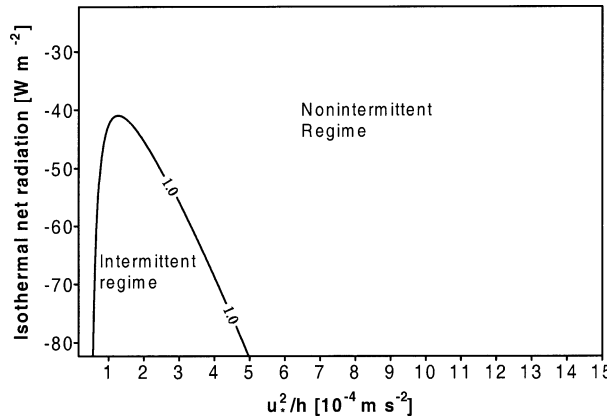


FIG. 8. As in Fig. 1, but with the horizontal axis in terms of u_*^2/h (6-h averages) instead of (effective) pressure gradient.

From now on, an axis as in Fig. 8 will be used. Adopting the assumptions above, the effective pressure gradient is estimated from the data by using 6-h-averaged values of the surface stress and of the boundary layer height (see section 4e).

It is, however, realized that many real SBLs do not show classical behavior. For example, Mahrt and Vickers (2002) show a number of CASES-99 nights where fluxes temporarily increase with height (upside-down boundary layers) before they decrease higher up. Also, SBL are often nonstationary by many causes, as with inertial oscillations. This means that Eq. (2) can, at best, only provide a crude approximation of the effective pressure gradient, limiting the generality of Fig. 8 (see discussion).

2) THE ISOTHERMAL NET RADIATION

A second key parameter determining the radiative forcing on the SBL system as defined in VdW(a,b) is the so-called isothermal net radiation (Monteith 1981; Holtslag and De Bruin 1988). The isothermal net radiation is defined as the net radiation that would occur if the near-surface layer were isothermal. This definition becomes clear by noting the linearized longwave radiation budget for the surface in the model (a small correction term is neglected):

$$Q_{\text{net}} \approx [-\sigma(\varepsilon_s - \varepsilon_a)T_{\text{ref}}^4 + N60] + 4\sigma T_{\text{ref}}^3(T_a - T_s). \quad (3)$$

This equation is derived by linearization of the original budget equation near a reference temperature T_{ref} [see VdW(a)]:

$$Q_{\text{net}} = \varepsilon_a \sigma T_a^4 + N60 - \varepsilon_s \sigma T_s^4. \quad (4)$$

By writing the net radiation equation as Eq. (3), it is clear that it can be divided in two parts: a part containing independent external parameters ε_a , ε_s , and cloud cover N (octa); and a part containing system variables T_a (air temperature) and T_s (surface temperature). The first part

of (3) is defined as the isothermal net radiation Q_i , because it equals the net radiation Q_{net} if $T_a = T_s$. For our dataset, Q_i is estimated from $Q_i = Q_{\text{net}} - 4\sigma T_{\text{ref}}^3(T_a - T_s)$, with T_a measured at 10 m, as in Table 1.

c. Local system parameters

An important parameter determining the vegetation–soil interaction is the so-called bulk conductance of the mulch/stagnant air layer within the vegetation [VdW(a)]. This bulk conductance is denoted with λ_m/δ_m $\text{W m}^{-2} \text{K}^{-1}$, where λ_m is the conductance (in $\text{W m}^{-1} \text{K}^{-1}$), and δ_m is the thickness of the mulch/stagnant air layer (in meters). It determines the heat flux through the vegetation layer, given a temperature difference between the vegetation top (radiation temperature T_s) and the soil surface (T_M):

$$G = (\lambda_m/\delta_m)(T_M - T_s). \quad (5)$$

For dense vegetation the bulk conductance can be easily determined by measuring G in combination with the radiation temperature of the vegetation T_s and the topsoil temperature T_M . In CASES-99, the surface was covered with dry, open prairie grass, so that bare soil was visible between the grass. Thus, the infrared camera (at 1.5 m), measures a composite of the vegetation top temperature T_s and the topsoil temperature T_M . If, for simplicity, we assume $\varepsilon_s = 1$ for both vegetation and bare soil, this can be approximated as

$$\sigma T_{\text{IRT}}^4 = A\sigma T_s^4 + (1 - A)\sigma T_M^4, \quad (6)$$

with $A[-]$, the fraction of vegetation cover. Regarding the approximation above, it is noted that the use of a slightly different power law (i.e., powers of 4.5 instead of 4) is probably more appropriate in the window region, although the results are very similar (within 1.5% error in $T_M - T_s$), that is, small compared to the uncertainties in the estimation of the vegetation fraction.

For a given vegetation fraction, the actual temperature of the vegetation top T_s can be calculated from the measured values T_{IRT} and T_M . Next, the value of G can be plotted as a function of $T_M - T_s$ in order to estimate the bulk conductance. In Fig. 9, this is applied to the CASES-99 data assuming two different values for the vegetation cover. The plots show surprisingly little scatter, given the strong empirical character of Eq. (5) not accounting for the complicated structure of real vegetation (leaf distribution/orientation). From Fig. 9, the following estimates for the bulk conductance are made (in $\text{W m}^{-2} \text{K}^{-1}$): $\lambda_m/\delta_m \approx 5$ for $A = 1.0$; $\lambda_m/\delta_m \approx 2$ for $A = 0.5$ [the intermediate case (not shown) gives $\lambda_m/\delta_m \approx 3.5$ using $A = 0.75$]. These “extremes” give a range for the bulk conductance at CASES-99. For comparison we note that Duynkerke (1999) found $\lambda_m/\delta_m \approx 3 \text{ W m}^{-2} \text{K}^{-1}$ for short, dense grass at Cabauw, comparable to the values given above.

Another vegetation parameter is the heat capacity C_v

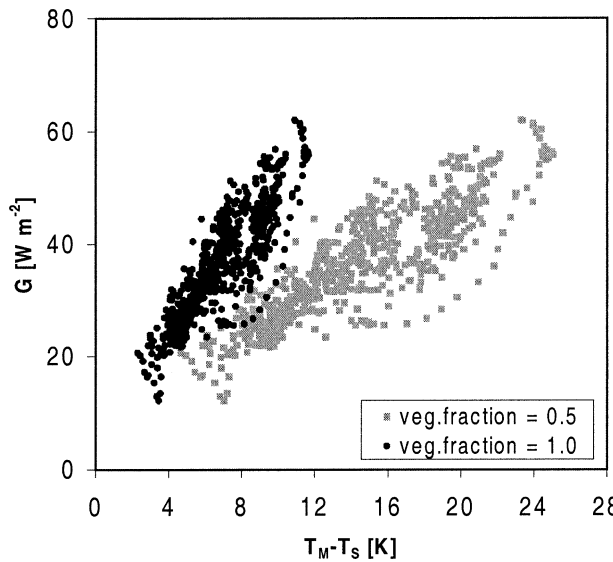


FIG. 9. Estimation of vegetation bulk conductance for two different fractions of vegetation cover.

of the vegetation top (per unit area). This parameter, which is difficult to estimate, was given an effective value of $2 \text{ kJ m}^{-2} \text{ K}^{-1}$ [as in VdW(a)], based on typical biomass estimations for grasslands (Atzema 1992), accounting for the dry and sparse character of the CASES-99 grass.

The momentum roughness length z_{0m} was taken to be 0.03 m, based on local measurements of momentum flux and wind profiles. In order to be consistent with the theoretical work, it was assumed that $z_{0m} = z_{0h}$. In future work this assumption could be refined.

d. Boundary conditions

1) BOTTOM BOUNDARY CONDITION FOR TEMPERATURE

In the simplified model the topsoil temperature T_M (the bottom system boundary) is assumed to be a known external variable, needed to calculate Π : T_M (at $z = 0.00$ m) is inferred from Fourier analysis of soil temperature measurements as explained in the appendix.

2) TOP BOUNDARY CONDITION FOR TEMPERATURE

In order to estimate the radiative forcing on the SBL system, strictly speaking, a temperature T_{TOP} at the boundary layer height is needed. As a practical approach, the temperature at the top of the central mast (55 m) was taken as T_{TOP} . Because, the strongest temperature gradient is usually below 55 m, Π is not very sensitive to the exact height at which this top temperature is evaluated as long as it is not close to the surface.

e. Other input parameters

BOUNDARY LAYER HEIGHT

From sodar observations at Beaumont, Oxford, and Whitewater [strength of the returned signal (in decibels)], a composite estimate of the boundary layer height (h) was made, given in Table 2. For a few cases, h was small enough (<55 m) to compare it with flux data from the central NCAR tower. Although the sodar estimates showed somewhat larger values than estimates from mast data, the comparison seemed reasonable for most cases. Generally, it is stressed, however, that the 6-h-averaged values of the h are rather crude estimates. In

TABLE 2. Overview of input parameters used for evaluation of Π . The calculated Π values are given for two values of λ_m/δ_m . (For explanation of class, see Table 1.)

DOY (-)	Date (-)	Time [LST (h)]	Class (-)	u_*^2/h (m s^{-2})	Q_i (W m^{-2})	h (m)	T_{TOP} (K)	T_M (K)	$\Pi \lambda_m/\delta_m$ = 5 (-)	$\Pi \lambda_m/\delta_m$ = 2 (-)
279	6 Oct	0000–0600	Int.	7.5E-05	-77.2	75	290.01	284.31	23.8	2.1
280	7 Oct	0000–0600	Turb.	1.3E-03	-80.8	145	290.59	286.98	268.3	258.6
281	8 Oct	0000–0600	Int.	1.7E-04	-56.0	115	290.78	287.48	19.2	-20.2
283	10 Oct	0000–0600	Rad.	6.8E-06	-67.3	70	294.15	287.53	86.0	56.0
284	11 Oct	0000–0600	Turb.	7.4E-04	-73.5	175	291.39	288.86	202.3	142.9
286	13 Oct	0000–0600	Trans.	7.5E-04	-78.2	150	295.03	291.28	152.1	102.9
287	14 Oct	0000–0600	Rad.	1.0E-05	-73.9	90	284.76	285.10	80.5	46.5
288	15 Oct	0000–0600	Turb.	1.2E-03	-84.5	200	294.82	290.05	366.5	358.5
290	17 Oct	0000–0600	Turb.	5.0E-03	-29.3	70	283.39	285.72	254.7	301.7
291	18 Oct	0000–0600	Int.	1.8E-04	-63.4	50	281.81	282.05	19.3	0.2
292	19 Oct	0000–0600	Rad.	1.6E-05	-70.2	70	282.98	283.28	56.9	31.4
293	20 Oct	0000–0600	Int.	8.1E-05	-73.0	61	284.50	281.63	22.5	3.4
294	21 Oct	0000–0600	Trans.	1.1E-04	-79.8	120	285.99	283.72	21.7	-18.5
295	22 Oct	0000–0600	Trans.	2.0E-04	-83.0	70	291.49	284.54	13.8	-8.0
296	23 Oct	0000–0600	Trans.	2.9E-04	-78.1	100	281.79	282.63	44.9	-5.2
297	24 Oct	0000–0600	Int.	1.0E-04	-70.1	52	280.89	281.01	20.9	2.7
298	25 Oct	0000–0600	Turb.	8.6E-04	-80.0	102	284.15	282.71	127.8	90.7
299	26 Oct	0000–0600	Rad.	1.1E-05	-83.8	30	291.05	283.04	40.5	27.1
300	27 Oct	0000–0600	Int.	2.5E-04	-85.3	100	291.89	285.83	16.9	-17.3
301	28 Oct	0000–0600	Trans.	4.1E-04	-71.4	130	290.83	287.28	55.0	0.9

some cases (e.g., 24 October), h showed considerable variation during the averaging period, responding to changing intensity of SBL turbulence. It is noted that the final results are not very sensitive to the exact value for h .

f. Summary

The total set of input parameters derived from the CASES-99 data is given in Table 2. Only days with a complete set of input parameters, derived from various instruments, could be analyzed. This limited the number of days. Additionally, the following constants were used $\varepsilon_s = 1.0$ (—), $\varepsilon_a = 0.8$ (—), $z_{0h} = z_{0m} = 0.03$ m, $T_{ref} = (T_{TOP} + T_m)/2$ K, and $C_v = 2$ kJ m⁻² K⁻¹. Unless stated otherwise, physical constants like Boltzmann's are given the same values as in VdW(a). Based on this input data, Π has been computed for two cases: $\lambda_m/\delta_m = 5$ (case 1), and 2 (case 2) (in W m⁻² K⁻¹). Before discussing the table results in the next section, we summarize explicitly the steps that are necessary to calculate Π . This in order to facilitate future application.

- 1) A list of input parameters [see also, overview Table 1 in VdW(a)] follows:
 - the effective pressure gradient (or, alternatively, u_*^2/h);
 - the isothermal net radiation Q_i [to be determined from Q_{net} and $(T_a - T_s)$, see section 4b];
 - the boundary layer height h , and the temperature at the boundary layer height T_{TOP} ;
 - the topsoil temperature T_m (see appendix);
 - estimations for the heat capacity C_v and the bulk conductivity λ_m/δ_m of the vegetation;
 - estimations for z_0 , ε_s , ε_a , and for a reference temperature T_{ref} ;
 - physical constants (standard notation), like σ , κ , and R_c .
- 2) Accounting for some scaling conversions and symbol definitions described explicitly in section 2 of VdW(b), the input parameters are substituted straightforwardly in the expressions for the equilibrium solutions of the system [VdW(b), appendix C].
- 3) Last, Π is found from substitution of this equilibrium solutions in the Π expression given in appendix D of VdW(b).

5. Comparison of theory and observations

a. Using full theory (Π)

In Fig. 10, the critical contour line $\Pi = 1$ from Fig. 8 is replotted. As before, this contour line is valid for a single location with a certain set of local parameters. Figure 10 (also the example in Fig. 8) is calculated for the CASES-99 site using local parameter estimations (e.g., z_{0m}) as given in the previous section. Because some of the parameters are not true physical constants

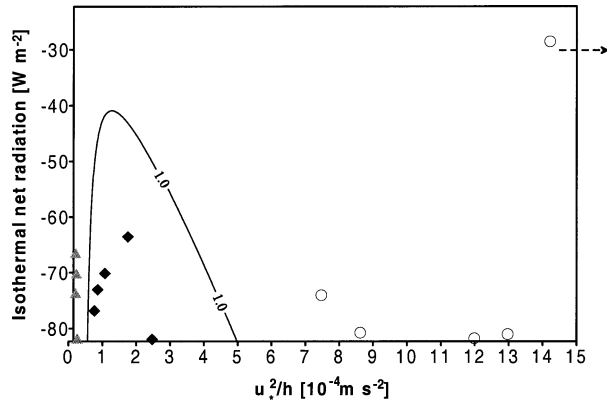


FIG. 10. Critical contour line $\Pi = 1$ for the CASES-99 site predicted by theory. Observed nights are located in this graph according to their values of Q_i and u_*^2/h . The nights are marked with different symbols according to their a priori time series classification described in section 3: gray triangles denote radiative nights; black diamonds, intermittent nights; and open circles, continuous turbulent nights (as in Fig. 11).

like T_m , T_{TOP} , and h they had to be given fixed values in order to plot this theoretical contourline. In Fig. 10 we assumed $T_m = T_{TOP} = 285$ K and $h = 80$ m.

For comparison, the CASES-99 nights are plotted in Fig. 10, according to their values of u_*^2/h and Q_i . The nights are marked with different symbols according to their a priori time series classification described in section 3. If we take the theoretical figure to be representative for the CASES-99 location (although, strictly speaking each night should have a slightly different contour line, due to the fact that each night has its own value of T_m , T_{TOP} , and h), then the observed nights with intermittent turbulence should be located within the contour line, and the nonintermittent nights should lie outside this contour line. Figure 10 shows that this is indeed the case, favoring the theoretical predictions (although the number of data points is limited). On the other hand, it is not clear how robust this result is in view of the assumptions and uncertainties in the parameter estimations. Therefore, a *sensitivity example* of the results in Fig. 10 is discussed below. First, however, some quantitative characteristics will be investigated.

Figure 10 represents a single contour line of a bowl-shaped figure (intermittent cases at the bottom of the bowl) showing Π as a function of u_*^2/h and Q_i . It would be interesting to know the exact Π values in Fig. 10; that is, what are the height of the observation points compared to the critical level ($\Pi = 1$)? First, we may simplify the representation of Fig. 10, by recognizing the fact that during CASES-99 clear-sky conditions prevailed over cloudy conditions. Thus, the isothermal net radiation was very similar for most of the nights, indicating that the dynamical differences between the nights are mainly caused by differences in u_*^2/h .

Therefore, we limit the parameter space by looking at Π as a function of u_*^2/h (Fig. 11a). Effectively, a

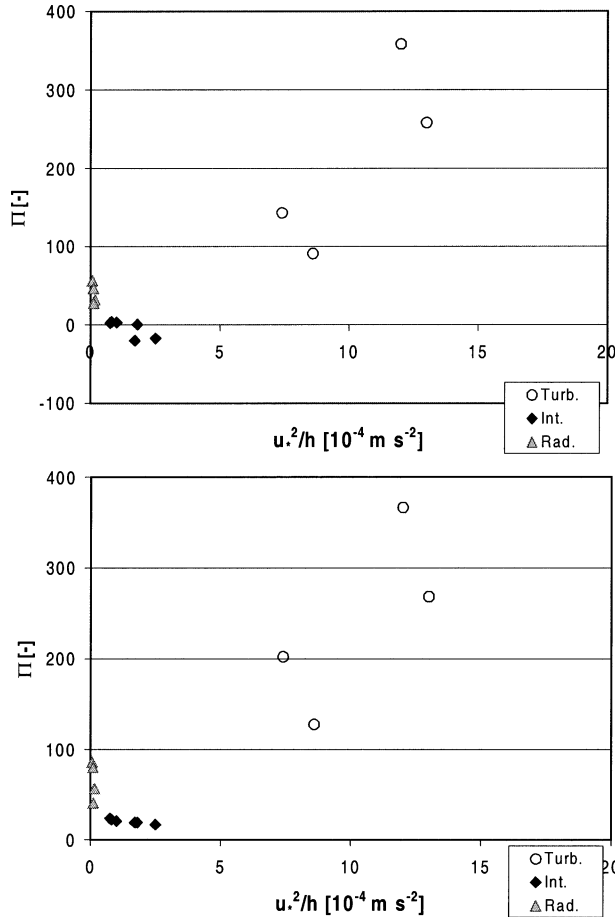


FIG. 11. Calculated Π values as a function of u_*^2/h for various CASES-99 nights [(top) with $\lambda_m/\delta_m = 2$; (bottom) with $\lambda_m/\delta_m = 5$].

horizontal slice is made in Fig. 10. The intersection of this slice with the contour line of Fig. 10 predicts the two pressure gradient values for which $\Pi = 1$ in Fig. 11a. Again, different symbols are used according to the a priori classification of section 3. In Fig. 11a it is shown that the nonintermittent nights show Π values larger than its critical value 1, and Π values below or just around the critical level coincide with observed intermittent nights, confirming the theoretical predictions of VdW(a,b). The data points do not exactly collapse on one single curve, due to small differences in Q_i , and differences in T_M , T_{TOP} , and h . But, roughly speaking, Figs. 11a and 10 indicate comparable results, confirming the predictive character of Π .

In Fig. 11b, the calculations of Π are identical to those in Fig. 11a, except for the fact that a bulk conductance λ_m/δ_m of $5 \text{ W m}^{-2} \text{ K}^{-1}$ is used, corresponding to a vegetation fraction of 1.0, instead of $\lambda_m/\delta_m = 2$ (vegetation fraction of 0.5). Although the qualitative shape of Fig. 11b is similar to that of Fig. 11a, its quantitative features are rather different. Figure 11b shows that, al-

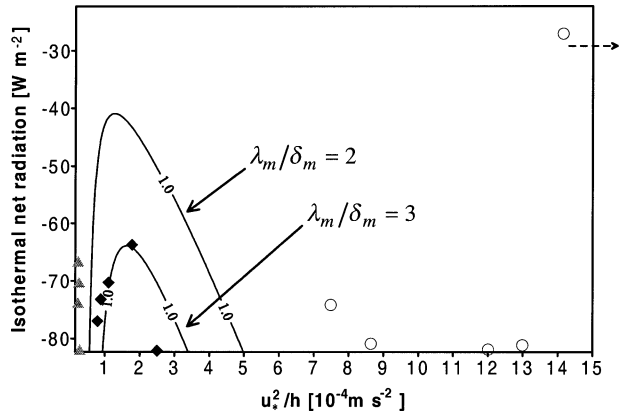


FIG. 12. As in Fig. 10, but for two values of λ_m/δ_m , namely, $\lambda_m/\delta_m = 2$ and $\lambda_m/\delta_m = 3 \text{ W m}^{-2} \text{ K}^{-1}$.

though the predicted Π values are low for the intermittent cases, they are not below the theoretical critical level of $\Pi = 1$, below which intermittency is predicted. Thus, although the observed intermittent cases are predicted to be most unstable (mathematically) of all, they are predicted just not unstable enough to be intermittent. The implications of this result for the general classifications Fig. 10 becomes clear in Fig. 12, showing two theoretical classifications for the CASES-99 site, using two different values of the bulk conductance. It is observed that the case with the highest bulk conductance ($\lambda_m/\delta_m = 3$) results in the smallest area with intermittent turbulence. The large value of λ_m/δ_m of $5 \text{ W m}^{-2} \text{ K}^{-1}$ (not shown) would not give a single Π value below the critical level 1 for any value of u_*^2/h and Q_i . As such, it could not be plotted as a contour line $\Pi = 1$. On the other hand, it is noted that even in this case of $\lambda_m/\delta_m = 5$, the most unstable cases are located in the same area as in the case of $\lambda_m/\delta_m = 2$ (as with Figs. 11a and 11b), indicating that the qualitative bowl-shaped dependence of Π remains unchanged. It is noted that the importance of the bulk conductance on the system stability was recognized/discussed in the previous studies of VdW(a,b).

In summary, although the regime predictions using this Π are robust and discriminative in a qualitative sense, the exact quantitative features have to be interpreted with caution, because of uncertainties in the parameter estimations.

b. A simplified approach

1) THEORETICAL BACKGROUND

A disadvantage of the Π parameter of VdW(b) is its complexity, which limits its applicability. Furthermore, due to this complexity this parameter does not provide insight in the physical cause of instability that generates intermittency. Therefore, in VdW(b), a less exact but simpler stability/classification criterion was given, which allows a physical interpretation. In this section,

this simplified criterion is applied to the CASES-99 dataset.

The approximate stability criterion (denoted as A-Cr.) is derived by application of a fixed shear criterion for instability (FSCI; Derbyshire 1999) to the surface energy balance equation. Here, only the result is given. The system is found to be mathematically/physically unstable (causing intermittency) when

$$\left(\frac{R_b}{R_c}\right)_{\text{eq}} > \frac{K + 1}{3}. \quad (7)$$

This criterion depends on two dimensionless groups

- the normalized equilibrium bulk Richardson number $(R_b/R_c)_{\text{eq}}$, and
- the partitioning parameter K .

Both groups are calculated from external variables. As expected, the equilibrium value of the bulk Richardson number is primarily determined by Q_i and by the effective pressure gradient. The second group, the so-called *partitioning parameter*, is physically interpreted as the ratio of the summed radiative and soil/vegetation conductance/exchange coefficient compared to the exchange coefficient for turbulent heat transport [VdW(b)]. If turbulent heat exchange were the only process involved, the criterion $(R_b/R_c)_{\text{eq}} > 1/3$ would imply a sufficient condition for system instability (assuming fixed shear). The discussion in the previous section, however, explained that a large soil heat flux (and additionally, the radiative flux) tends to stabilize the system, counteracting intermittency. This effect is accounted for in the partitioning parameter, making $(R_b/R_c)_{\text{eq}} > 1/3$ a necessary but not a sufficient condition.

For the application of the A-Cr., external parameters were estimated as with Π except for the following.

- T_{TOP} and T_M are not needed as input parameters.
- Instead, at the bottom boundary, G is needed as input. Because G was only available for a limited number of days (Table 2), G is estimated from the residual of the other energy balance terms, accounting for the gap in the energy balance closure (13 W m^{-2}).

2) RESULTS

For the available CASES-99 nights, both terms in the stability criterion of Eq. (7) were calculated (Fig. 13). Moreover, the *difference* between those two terms, $(R_b/R_c)_{\text{eq}} - (K + 1)/3$, is plotted, marked differently according to the a priori classification based on the flux time series, as in Figs. 11a,b. A positive difference means $(R_b/R_c)_{\text{eq}} > (K + 1)/3$, predicting instability (causing intermittency). Likewise, a negative difference predicts a nonintermittent situation.

To some extent the system stability is predicted correctly: negative differences coincide with radiative and turbulent nights, and the intermittent nights show pos-

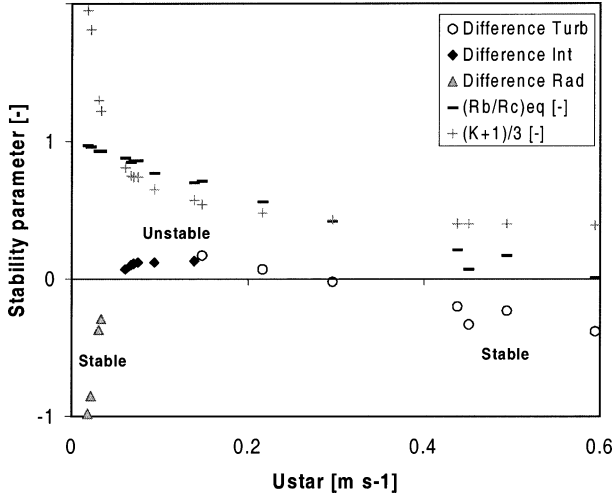


FIG. 13. The simplified stability parameter, indicated as the difference $(R_b/R_c)_{\text{eq}} - (K + 1)/3$, as a function of u_* . Different symbols are used (as in Fig. 10) according to the a priori classification (section 3). Separate terms of the stability parameter are given by dashes and crosses.

itive values. However, the “in between” cases show that some turbulent nights are incorrectly predicted as being unstable. Moreover, the slope between the intermittent and turbulent cases is rather flat, indicating that the figure is not very discriminative for these cases (contrary to the strong slopes in Figs. 11a,b). It is noted that the use of a larger bulk conductance, λ_m/δ_m of 5 instead of 2 $\text{W m}^{-2} \text{ K}^{-1}$, gave very similar results as with Π , that is, leading to system stabilization.

In summary, although the approximate criterion provides useful physical insight and predicts the extreme cases correctly, its predictions are incorrect or not very discriminative for the more subtle cases. For these cases the basic fixed shear assumption is probably not correct (Derbyshire 1999). Therefore, for these cases, the momentum equation needs to be accounted for in a coupled momentum–energy balance system as in the derivation of Π .

6. Discussion

a. Quantitative/qualitative features

The previous sections showed that the predictions with Π are robust in a qualitative sense: intermittency is most likely to occur under clear-sky conditions in presence of a moderately/weak pressure gradient, in agreement with what is generally observed (section 3). This robustness can be understood from the basic mechanism [see introduction; VdW(a,b)], which needs two basic ingredients: 1) a positive feedback of stratification on turbulent mixing, enabling decoupling; and 2) a pressure gradient that accelerates the flow after decoupling, enabling recoupling. In conditions of strong winds and/ or large cloud cover the Richardson numbers are too

low to generate decoupling (no positive feedback, see Fig. 5) so that no intermittency will occur. In the other extreme, in the absence of a significant pressure gradient, the flow acceleration is either absent or not strong enough to generate intermittency.

Despite this qualitative robustness, our results [especially VdW(a)] indicate a large sensitivity of the Π value on (uncertain) parameter estimations. This means that a single Π value on itself cannot be interpreted as a reliable predictor of intermittent/nonintermittent SBL regimes. Rather, the *relative* value of Π compared to the Π values of other nights at the same location (under various conditions) tells more about the probability of finding a particular regime during this night. This result indicates that the qualitative/conceptual value of the present study is more important than its direct quantitative significance. This is certainly true in the light of the rather strict model assumptions.

b. Other classifications

The present paper tries to express/predict different SBL regimes in terms of *external forcing parameters* such as pressure gradient and cloud cover. First, it is believed that, eventually, these external parameters determine SBL behavior [apart from the discussion on predictability by McNider et al. (1995)]. Second, especially in the intermittent regime, external parameters tend to vary less than internal system parameters, like wind speed, temperature, u_* , L , etc. Section 4, however, shows that in practice, still internal input parameters such as u_*^2/h , h itself, T_M , and T_{TOP} , are needed (albeit using 6-h averages) to calculate Π . By inclusion of more model complexity in future studies, some of these internal variables could be related to external parameters. For example, the inclusion of Coriolis effects (separate U and V equations) translates the *effective* pressure gradient into a real pressure gradient as input parameter.

In literature SBL classifications have been proposed using *internal system parameters* such as z/L , z/Λ , h/L , and z/h , based on similarity arguments (Holtslag and Nieuwstadt 1986). Using z/L as an indicator, Mahrt et al. (1998) classified the stable surface layer into (a) weakly stable, (b) moderately stable, and (c) very stable. Although this classification proved to be very useful as a guideline to look at surface layer observations, it is not meant as an *exact* predictor of different SBL regimes (here, especially the intermittent regime). Generally speaking, the studies mentioned above indicate that intermittent turbulence is most likely at large stability conditions, that is, large values of Ri , z/Λ , z/L , or h/L . This fact is confirmed by the present study and others (e.g., Kondo et al. 1978; Howell and Sun 1999). Additionally, the present study stresses the importance of other heat exchange processes (besides turbulence) such as soil/radiative heat flux, that stabilize SBL intermittency.

c. Future research

It would be interesting to extend the present work, in a sense of analyzing SBL regimes in relation to external forcing parameters, to larger datasets (including cloudy cases), and for different types of land cover (with different physical properties). With this respect the authors suggest that a closer collaboration between NWP modelers and experimentalists will benefit these type of classification studies (particularly in relation to an accurate diagnosis of pressure gradients; see section 4b).

Apart from the present system analysis approach using a simplified model, there is need for more detailed studies on intermittency dynamics. Although the intermittency mechanism arising from a positive feedback between stratification and mixing efficiency in shear flow is an important candidate explaining the observed intermittency in SBLs, it is not clear whether this intermittency is caused by a direct surface-atmosphere interaction (present work), is formed in shear layers higher up (e.g., Coulter 1990; Ha and Mahrt 2001), or is a combination of both. It is challenging to extend the present work (both the theoretical and observational part) to the more general case, allowing both atmosphere-surface interaction and interaction with higher shear layers.

7. Conclusions

In this paper a classification of intermittent and nonintermittent turbulence is presented based on observations of near-surface turbulence during CASES-99. It is found that the different nights can be subdivided in three subclasses: 1) a turbulent regime, 2) an intermittent regime, or 3) a radiative regime. These classes reflect different SBL dynamics. Moreover, the existence of three regimes confirms the findings of VdW(a) who simulated three different SBL regimes with a simplified model.

This bulk model of VdW(a) showed both intermittent and nonintermittent SBL behavior for different parameter ranges. In VdW(b), analysis of the model equations resulted in a dimensionless number (Π), which is a function of external forcing parameters such as the (effective) pressure gradient and the radiative forcing. With this number, the model behavior (i.e., intermittent or nonintermittent) could be predicted.

The present study uses this parameter to classify/predict intermittent and nonintermittent nights at CASES-99. To this end, Π was evaluated from detailed analysis of the available data. Comparison of the predictions/classification using Π , with the actual observed regimes shows generally good agreement.

- Those nights predicted to be most (mathematically) unstable to disturbances, turned out to be intermittent.
- The most stable (mathematically) nights turned out to be nonintermittent, that is, continuously turbulent or radiative.

The qualitative features mentioned above are very robust and discriminative. Thus, under the assumptions made, the Π concept could be useful as a classification tool.

The exact quantitative value of Π shows to be rather sensitive to local parameters such as the bulk conductance of the vegetation layer, which is difficult to estimate exactly *a priori*. In practice, this makes Π unsuitable as an *absolute* predictor of stability/SBL regimes. However, useful information about the stability/regime of a particular night is obtained by comparing its Π value *relative* to other nights under different conditions.

In VdW(b) an approximation for the rather complex Π was derived. This approximation based on a fixed shear criterion for instability provided new insight in the relative importance of the different boundary layer processes (turbulence, radiation, soil conduction) in the instability mechanism [VdW(b)]. As in the Π case, the regime predictions are compared with the observed regimes. The approximate parameter correctly predicts extreme cases. However, in the more subtle cases the approximation shows to be less decisive or even incorrect, probably due to the fact that the fixed shear assumption is not a good approximation for these cases.

In light of the present work, it seems useful to investigate the occurrence of stable boundary layer regimes in relation to their external forcing parameters. As such, classification diagrams like Figs. 1 and 10 may provide a new conceptual perspective for future (observational and modeling) work on SBL regimes.

APPENDIX

Fourier Analysis of Soil Temperatures

To solve the surface energy balance one would like to measure the soil heat flux (SHF) directly at the soil surface. In practice this is often not possible without disturbing the surface properties, due to the presence of vegetation/roots. Therefore, the SHF is often measured a few centimeters below the soil surface. Thus, the mea-

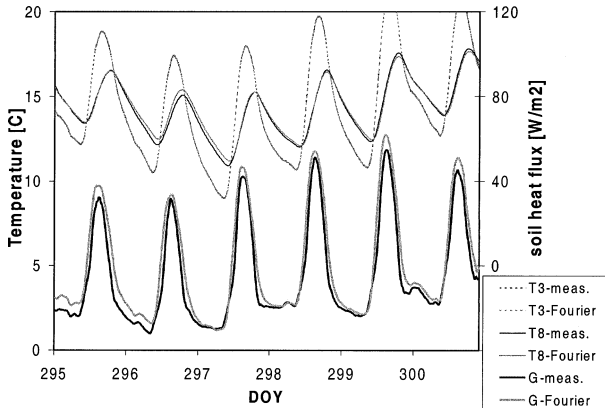


FIG. A1. Measured and modeled soil temperatures/fluxes.

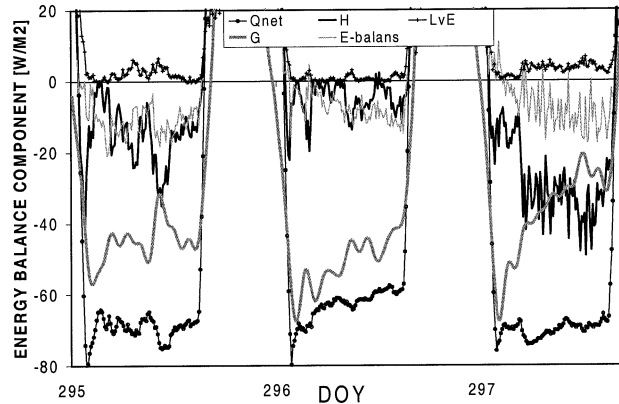


FIG. A2. Energy balance components in three typical nights.

sured values need to be extrapolated to the surface in a consistent way. A method is given below. For a detailed background of the theory we refer to van Wijk and de Vries (1963).

In the analysis, data from thermometers at -3 and -8 cm and an SHF plate at -5.4 cm are used, available during DOYs 289–301. The time series of the 3-cm temperature is decomposed in 150 Fourier components, which results in a nearly perfect fit (Fig. A1). Using standard theory of heat conduction (assuming homogeneity) the temperature signal at 8-cm depth is reconstructed (Fig. A1) using a “best fit” thermal diffusivity value κ_{th} . For our set this gave $\kappa_{th} = 0.155 \times 10^{-6} \text{ m}^2 \text{ s}^{-1}$, comparable to values for dry sand ($0.24 \times 10^{-6} \text{ m}^2 \text{ s}^{-1}$) and clay ($0.18 \times 10^{-6} \text{ m}^2 \text{ s}^{-1}$; Oke 1978). Knowing this κ_{th} value, $T(z, t)$ is known for every z, t assuming homogeneity of soil properties in space/time. In this way $T_8(t)$ was found substituting $z = 0$ (section 4).

Next, the SHF at 5.4-cm depth is reconstructed (Fig. A1) by differentiating $T(z, t)$ with respect to z , assuming a best fit value for the soil conductivity λ_s of $0.6 \text{ W m}^{-1} \text{ K}^{-1}$. With this λ_s value, $G(z, t)$ is known and the SHF at the surface $G(0, t)$ is found by substituting $z = 0$. The result is shown in Fig. A2, which gives an overview of the energy balance for three typical nights. Comparing Figs. A2 and A1 shows that both the magnitude and the shape of $G(0, t)$ has changed a lot compared to the original measured $G(-0.054, t)$, indicating the importance of the extrapolation.

An innovative element of this study are large temporal changes in $G(0, t)$, which are realistic features: the soil heat flux not only reacts on the peak value of the net radiation at the beginning of the night, but also reflects the intermittent behavior of the turbulent heat flux at DOY 296, and the “jump” in the heat flux at DOY 297. As such, strong fluctuations cancel out in the final energy balance budget. Apparently, the intermittent character in the turbulent flux is transferred into the soil and is still noticeable in the temperature measurements, despite its apparently smooth time series (A1).

REFERENCES

- Atzema, A. J., 1992: A model for the drying of grass with realtime weather data. *J. Agric. Eng. Res.*, **53**, 231–247.
- Blackadar, A. K., 1979: High-resolution models of planetary boundary layer. *Advances in Environmental Science and Engineering*, J. R. Pfaffen and E. N. Ziegler, Eds., Gordon and Breach, 50–85.
- Businger, J. A., 1973: Turbulent transfer in the atmospheric surface layer. *Workshop on Micrometeorology*, D. A. Haugen, Ed., Amer. Meteor. Soc., 67–100.
- Coulter, R. L., 1990: A case study of turbulence in the stable nocturnal boundary layer. *Bound.-Layer Meteor.*, **52**, 75–91.
- De Bruin, H. A. R., 1994: Analytic solutions of the equations governing the temperature fluctuation method. *Bound.-Layer Meteor.*, **68**, 427–432.
- Derbyshire, S. H., 1999: Boundary-layer decoupling over cold surfaces as a physical boundary instability. *Bound.-Layer Meteor.*, **90**, 297–325.
- Duynderke, P. G., 1999: Turbulence, radiation and fog in Dutch stable boundary layers. *Bound.-Layer Meteor.*, **90**, 447–477.
- Ha, K.-J., and L. Mahrt, 2001: Simple inclusion of z-less turbulence within and above the modeled nocturnal boundary layer. *Mon. Wea. Rev.*, **129**, 2136–2143.
- Hartogensis, O. K., H. A. R. De Bruin, and B. J. H. van de Wiel, 2002: Displaced-beam small aperture scintillometer test. Part II: CASES-99 stable boundary layer experiment. *Bound.-Layer Meteor.*, **105**, 149–176.
- Holtslag, A. A. M., and F. T. M. Nieuwstadt, 1986: Scaling the atmospheric boundary layer. *Bound.-Layer Meteor.*, **36**, 201–209.
- , and H. A. R. De Bruin, 1988: Applied modelling of the nighttime surface energy balance over land. *Bound.-Layer Meteor.*, **27**, 689–704.
- Howell, J. F., and J. Sun, 1999: Surface-layer fluxes in stable conditions. *Bound.-Layer Meteor.*, **90**, 495–520.
- Kondo, J., O. Kanechika, and N. Yasuda, 1978: Heat and momentum transfers under strong stability in the atmospheric surface layer. *J. Atmos. Sci.*, **35**, 1012–1021.
- Lin, J. T., 1990: The effect of inertial and turbulence oscillations in the stable boundary layer and their role in horizontal dispersion. M.S. thesis, Dept. of Mathematics, University of Alabama in Huntsville, 82 pp.
- Mahrt, L., 1999: Stratified atmospheric boundary layers. *Bound.-Layer Meteor.*, **90**, 375–396.
- , and D. Vickers, 2002: Contrasting vertical structures of nocturnal boundary layers. *Bound.-Layer Meteor.*, **105**, 351–363.
- , J. Sun, W. Blumen, T. Delany, and S. Oncley, 1998: Nocturnal boundary layer regimes. *Bound.-Layer Meteor.*, **88**, 255–278.
- McNider, R. T., D. E. England, M. J. Friedman, and X. Shi, 1995: Predictability of the stable atmospheric boundary layer. *J. Atmos. Sci.*, **52**, 1602–1614.
- Monteith, J. L., 1981: Evaporation and surface temperature. *Quart. J. Roy. Meteor. Soc.*, **107**, 1–27.
- Moore, C., 1986: Frequency response corrections for eddy correlation systems. *Bound.-Layer Meteor.*, **37**, 17–35.
- Nappo, C., 1991: Sporadic breakdown of stability in the PBL over simple and complex terrain. *Bound.-Layer Meteor.*, **54**, 69–87.
- Nieuwstadt, F. T. M., 1984: The turbulent structure of the stable, nocturnal boundary layer. *J. Atmos. Sci.*, **41**, 2202–2216.
- , and H. Tennekes, 1981: A rate equation for the nocturnal boundary-layer height. *J. Atmos. Sci.*, **38**, 1418–1428.
- Oke, T. R., 1978: *Boundary Layer Climates*. Methuen and Co., 372 pp.
- Poulos, G. S., and Coauthors, 2002: CASES-99: A comprehensive investigation of the stable nocturnal boundary layer. *Bull. Amer. Meteor. Soc.*, **83**, 555–581.
- Revelle, D. O., 1993: Chaos and “bursting” in the planetary boundary layer. *J. Appl. Meteor.*, **32**, 1169–1180.
- Turner, J. S., 1973: *Bouyancy Effects in Fluids*. Cambridge University Press, 368 pp.
- Van de Wiel, B. J. H., R. J. Ronda, A. F. Moene, H. A. R. De Bruin, and A. A. M. Holtslag, 2002a: Intermittent turbulence and oscillations in the stable boundary layer over land. Part I: A bulk model. *J. Atmos. Sci.*, **59**, 942–958.
- , A. F. Moene, R. J. Ronda, H. A. R. De Bruin, and A. A. M. Holtslag, 2002b: Intermittent turbulence and oscillations in the stable boundary layer over land. Part II: A system dynamics approach. *J. Atmos. Sci.*, **59**, 2567–2581.
- van Wijk, W. R., and D. A. de Vries, 1963: Periodic temperature variations. *Physics of Plant Environment*, W. R. van Wijk, Ed., Interscience, 133–138.